Supplementary Information for

Light bulb-inspired high-temperature catalytic depolymerization of polyolefin plastic with high monomer selectivity

Shijie Yu[1,4], Peijie Han[1,4], Haoyue Li[1], Sikai Wang[1], Junyang Xuan[1], Ning Yan[1,2,3]*

[1]*Department of Chemical and Biomolecular Engineering, National University of Singapore, Singapore 117585, Singapore*

[2]*Joint School of National University of Singapore and Tianjin University, Fuzhou 350207, Fujian, China*

[3]*Centre for Hydrogen Innovations, National University of Singapore, Singapore 117585, Singapore*

[4]*These authors contributed equally.*

**Corresponding author: ning.yan@nus.edu.sg (NY)*

Supplementary Methods

Materials

Low-molecular-weight polyethylene, high-molecular-weight polyethylene, and polypropylene were purchased from Sigma-Aldrich. Metal filaments were obtained from Goodfellow Cambridge Ltd., Tengfeng Metal Materials Ltd., Fuxiang Metal Materials Ltd., Keyannuo New Material Technology Ltd., Frank New Materials Ltd., Shanghai Rush Metal Co., Ltd, Guantai Metal Materials Ltd. Argon, nitrogen, ethylene, and a standard gas mixture with methane (CH_4, 1%), ethane (C_2H_6, 0.5%), ethylene (C_2H_4, 1%), ethyne (C_2H_2, 1.5%), propane (C_3H_8, 0.5%), propylene (C_3H_6, 1%), propyne (C_3H_4, 1.5%), and nitrogen (N_2, 93%) were obtained from Air Liquide.

Depolymerization experiment

In a typical experiment, the surface of the metal filament is coated with plastic through the in-situ Joule heating effect of the metal filament (Fig. S1). The ends of the metal filament were then secured to the OT-type open-end copper fittings. The copper fittings at each end were bolted to the copper wire connectors in the flange seals on each side. The outer end of the copper wire was directly connected to a small direct current (DC) power supply for subsequent lighting of the metal filament. The entire plastic-coated metal filament was placed in the center of a cylindrical quartz tube with an inner diameter of 20 mm, and the metal filament was secured and adjusted on both sides by means of copper wires. The quartz tube was sealed to the flange seals by four fluorinated rubber O-rings. On the other side of the inlet flange seal a tee line was connected, one of which was used for the connection of the copper wires and the other for feeding the carrier gas into the reactor. The flange seal at the outlet was similar, and the tee line was used for the

transmission of the circuit and the outflow and collection of the gas. After installing the reaction apparatus, the reactor inlet was first closed, and a vacuum pump was connected to the outlet. The vacuum pump was turned on to remove air from inside the reactor and the vacuum inside the reactor was balanced with argon gas from upstream and repeated five times. Afterward, the reactor was steadily fed with an argon carrier gas for one hour to ensure the removal of impurity gases, such as oxygen, from the reaction chamber. Next, a small DC power supply was turned on to illuminate the metal filament. The temperature of the metal filament was measured by the Optris PI 05M infrared camera and verified by the difference in resistance at room temperature and during operation and the corresponding resistance temperature coefficient [1,2]. A gas sample bag was attached to the back end of the reactor for the collection and analysis of products. The gas products were then passed into an Agilent 8890 gas chromatography with flame ionization detection (GC-FID) for detection. The products were separated on a GS-Alumina KCl porous layer open tubular (PLOT) column (Agilent Technologies Inc., 50 m × 0.530 mm).

Characterization

The elemental composition (C, H, N, and S) was determined via a ThermoFisher Scientific FlashSmart CHNS Elemental Analyser. The analysis was accomplished using a modified DUMAS method [3,4]. Samples were first weighed in a tin container. The sample was then burned with oxygen at high temperatures, and the resulting gases were carried out by a helium gas stream and passed through a gas chromatography column attached to a thermal conductivity detector (TCD) for the determination of specific elements.

Raman spectra were collected in the spectral range of 500–3500 cm^{-1} using a Renishaw inVia Qontor confocal Raman microscope outfitted with a Renishaw Centrus 4AUL40 detector. A ×50

objective lens was used to collect all spectra with a 532 nm edge laser (power 10%) and a grating of 1800 l/mm (vis). For each sample, Raman spectroscopy was measured at a different physical location to ensure sample homogeneity, repeated four times.

X-ray photoelectron spectroscopy (XPS) was carried out in a Kratos AXIS ULTRA^{DLD} instrument (Shimadzu, Japan) at a working pressure of 5×10^{-9} Torr with an optimal energy resolution of less than 0.73 eV. Mono Al Kα X-rays (1486.71 eV, 5mA, 15 kV) were used as the radiation source, and the photoelectrons were analyzed using a hemispherical sector analyzer (HSA). For a survey scan, the pass energy is 160 eV. For a narrow scan, the pass energy is 40 eV. The C–C component of C 1s (285.0 eV) was used for the calibration [5].

^{1}H magic-angle spinning (MAS) solid-state nuclear magnetic resonance (NMR) spectroscopy measurements were conducted on a Bruker Avance NEO 500MHz NMR spectrometer using a commercial 4 mm probe. A sample spinning rate of ~12 kHz was used to produce a high-resolution MAS NMR spectrum. ^{13}C cross-polarization (CP)/MAS/total suppression of sidebands (TOSS) solid-state NMR spectroscopy measurements were conducted on a Bruker Avance NEO 500MHz NMR spectrometer using a commercial 4 mm probe. A sample spinning rate of ~8 kHz was used to produce a high-resolution CP/MAS/TOSS NMR spectrum.

Molecular weight distributions were analyzed on an Agilent PL-GPC 220 high-temperature gel permeation chromatography (HT-GPC), equipped with two PLgel 10 μm MIXED-B columns and a refractive index (RI) detector. Samples were dissolved in 1,2,4-trichlorobenzene (TCB) by heating at 150 °C. Elution was performed using TCB at 150 °C with a flow rate of 1.0 mL min^{-1}.

The microscopic morphology was observed through a JSM-7610F Plus (JEOL, Japan) scanning electron microscopy (SEM) with a secondary electron image (SEI) mode. The elemental

distribution was examined by X-Max^N (Oxford Instruments, UK) energy dispersive X-ray spectroscopy (EDS) with a resolution of 5.9 keV.

Computational fluid dynamics simulation

A three-dimensional transient computational fluid dynamics (CFD) simulation was carried out in order to obtain the distribution and variation of the temperature and flow fields in the reaction space. This CFD numerical simulation was implemented based on Ansys Fluent software. The physical parameters used in this numerical model are listed in Table S8 unless otherwise noted. The effect of gravity was considered throughout the numerical simulation. The heat transfer effects of conduction, convection, and radiation were considered simultaneously when performing heat and temperature calculations, and radiation was simulated using the discrete ordinates (DO) radiation model. The emissivity of the tungsten filament varies with temperature and was calculated according to the following equation [6-8]:

$$\varepsilon_t = \varepsilon_0 \left(\frac{T}{T_0}\right)^{\left(-0.13222\frac{T}{1000}+1.765\right)} \quad \text{(S1)}$$

where ε_0 represents the emissivity of tungsten filament at room temperature with a value of 0.0145 and T_0 represents room temperature, respectively.

The boundary condition at the outer wall of the quartz tube was set to natural convection of air at room temperature. A laminar flow model was used in the CFD numerical simulation to simulate the distribution and variation of the flow field. The gas was modeled as an ideal gas. The simulation of the flow field was based on the basic equations of fluid mechanics, including the equation of continuity, the equation of momentum conservation, and the equation of energy conservation.

Density function theory calculation

Density function theory (DFT) calculations for the gas-phase reaction were performed with the Gaussian 16 program package [9]. All species involved in radical-induced gas-phase pathways were optimized at the B3LYP/6-311+G(d, p) level of theory [10], and the corresponding transition states were confirmed by the number and vibration direction of their virtual frequencies. Dispersion correction was taken into account during geometrical optimization by applying Grimme's D3BJ method [11]. Temperature and pressure were set to be 1523 K and 1 atm, respectively, for Gibbs free energy calculations by using Multiwfn (version 3.6) [12], which are consistent with the experimental reaction condition of this study.

The structural data of Co (a = b = 2.47 Å, c = 4.02 Å), Fe (a = b = c = 2.86 Å), Ir (a = b = c = 3.85 Å), Mo (a = b = c = 3.17 Å), Nb (a = b = c = 3.32 Å), Ni (a = b = c = 3.48 Å), Pd (a = b = c = 3.92 Å), Pt (a = b = c = 3.94 Å), Re (a = b = 2.77 Å, c = 4.47 Å), Ta (a = b = c = 3.31 Å), Ti (a = b = 4.57 Å, c = 2.83 Å), V (a = b = c = 2.98 Å), W (a = b = c = 3.17 Å), and Zr (a = b = 3.24 Å, c = 5.17 Å) were obtained from the website of Materials Project [13] before crystal optimization. A 4 × 4 Co (001) with 5 layers, 3 × 3 Fe (110) with 5 layers, 2 × 2 Ir (111) with 5 layers, 3 × 3 Mo (110) with 5 layers, 4 × 2 Nb (110) with 5 layers, 2 × 2 Ni (111) with 5 layers, 2 × 2 Pd (110) with 6 layers, 2 × 2 Pt (111) with 5 layers, 4 × 4 Re (001) with 5 layers, 3 × 2 Ta (110) with 5 layers, 2 × 2 Ti (001) with 6 layers, 3 × 3 V (110) with 5 layers, 3 × 2 W (110) with 5 layers, and 4 × 4 Zr (001) with 5 layers were constructed as slab models. The bottom 3 layer were fixed to simulate the bulk properties, while the remaining layers and molecules were allowed to relax. The vacuum thickness of all slab models was 15 Å. The structure of the hydrogen atom in the vacuum was calculated using a 15 × 15 × 15 Å unit cell.

All periodic DFT calculations were carried out using the Vienna ab initio simulation package (VASP) [14-17] with the Perdew−Burke−Ernzerhof (PBE) exchange-correlation functional [18]. A plane wave basis set with an energy cutoff of 400 eV was used. Brillouin zone integration was performed using Γ-only k-point mesh and Gaussian smearing of 0.05 eV. Grimme's dispersion correction was employed during each geometry optimization step [19]. All structures were refined until the Hellman-Feynman forces on each ion were lower than 0.05 eV/Å.

The adsorption energies (ΔE_{ads}) of C_6H_{14} on the surface was calculated as follows:

$$\Delta E_{ads} = E_{slab+\ C6H14} - E_{slab} - E_{C6H14} \quad \text{(S2)}$$

where E_{slab+i}, $E_{slab,}$ and $E_{\ C6H14}$ are DFT-calculated energies of the adsorption complex, the clean metal slab, and gas-phase C_6H_{14} molecule, respectively.

Preparation and characterization of polyethylene after treatment

Polyethylene was treated by heating the polyethylene to a molten state under an air atmosphere for 100 hours. This was used for verification of the potential industrial feasibility of the polyethylene melt pool. Molecular weight distributions of the treated polyethylene were analyzed on an Agilent PL-GPC 220 HT-GPC, equipped with two PLgel 10 μm MIXED-B columns and a RI detector. Samples were dissolved in TCB by heating at 150 °C. Elution was performed using TCB at 150 °C with a flow rate of 1.0 mL min^{-1}.

Life cycle assessment

The goal of the life cycle assessment (LCA) is to assess the environmental impacts of the different methods for polyolefin plastic recycling or treatment. Four scenarios were considered in this study, including this work, mechanical recycling, incineration, and pyrolysis. The functional

unit is the treatment of 1 tonne of polyolefin plastic. The tungsten filament scenario includes the following processing blocks: grinding of polyolefin plastics products into plastic powder, coating of polyolefin plastics powder, and depolymerization of polyolefin plastics. The mechanical recycling scenario includes the following processing blocks: grinding of polyolefin plastics products into plastic powder, fabrication and extrusion of the plastic powder into recycled plastic products. The incineration scenario is considered to contain only the incineration of polyolefin plastics. The pyrolysis scenario includes the following processing blocks: grinding of polyolefin plastics products into plastic powder and pyrolysis of the plastic powder. The life cycle inventory (LCI) data for inputs were primarily sourced from the Argonne National Laboratory GREET Model and Ecoinvent database (v3.8). When not available in these databases, relevant LCI data were calculated from the electricity of energy consumption based on Argonne National Laboratory GREET Model or obtained from some representative literature [20-22]. ReCiPe2016 (H) was applied in the life cycle impact assessment (LCIA). Three environmental impacts were considered in this work, including energy consumption, greenhouse gas (GHG) emission, and water consumption.

Supplementary Figures

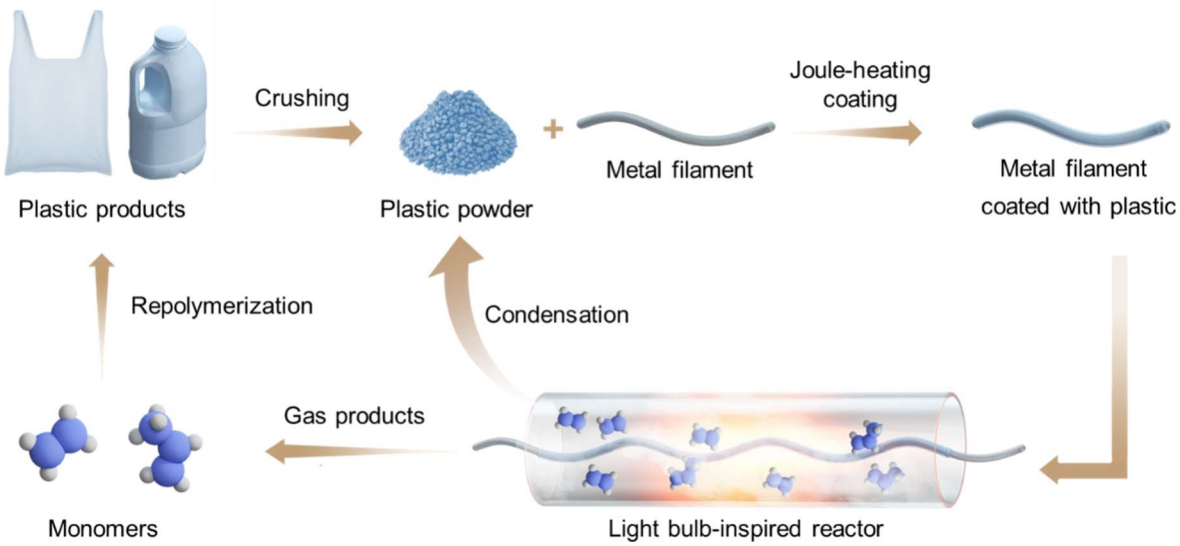

Fig. S1. Technological route of assembly and depolymerization of plastic in the light bulb-inspired reactor.

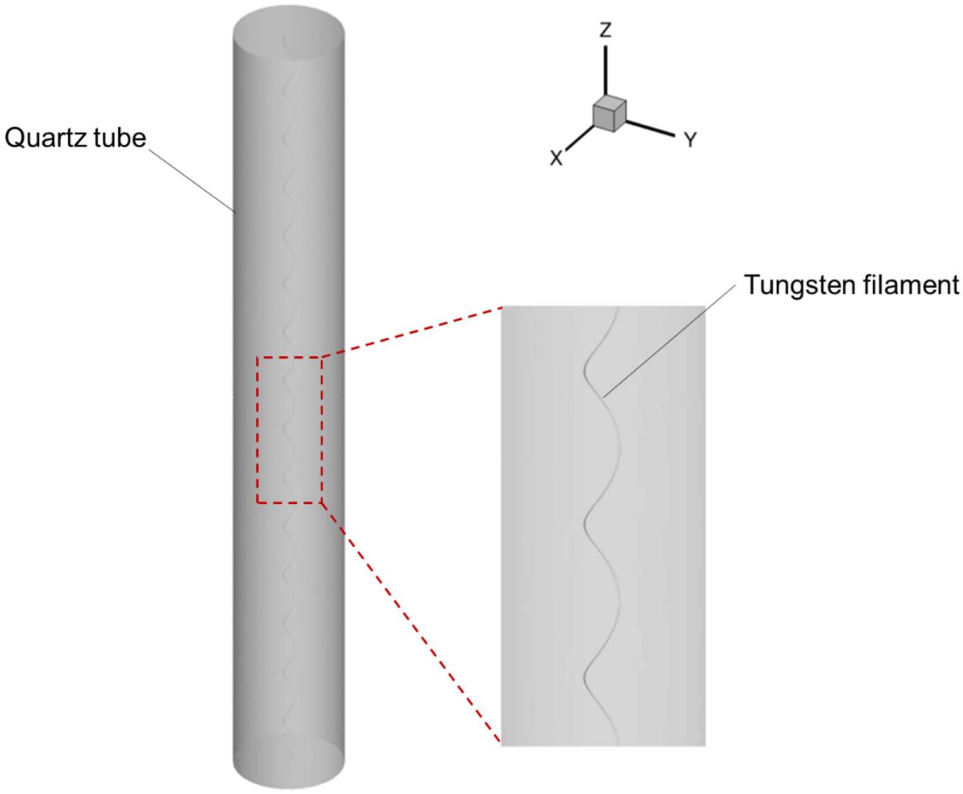

Fig. S2. Schematic diagram of the light bulb-inspired reactor.

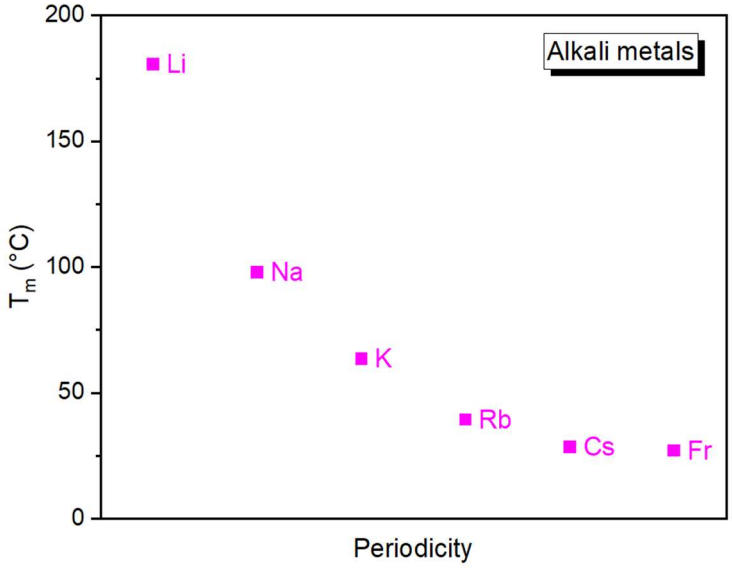

Fig. S3. The melting points of different metals in alkali metals.

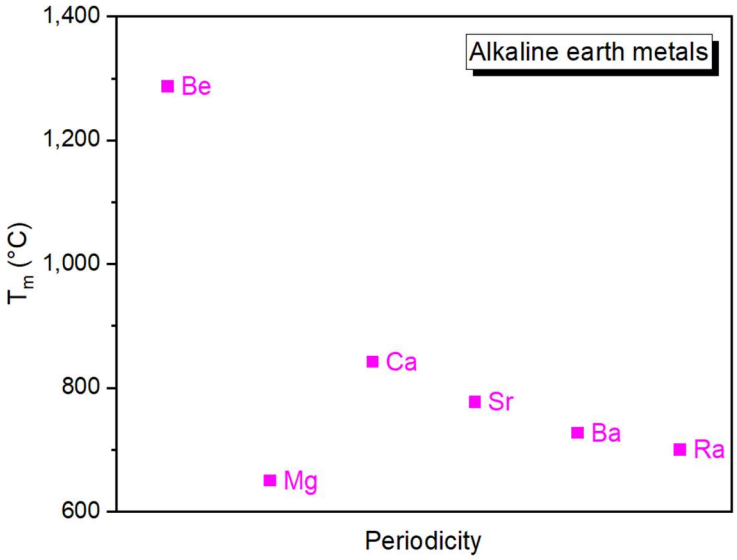

Fig. S4. The melting points of different metals in alkaline earth metals.

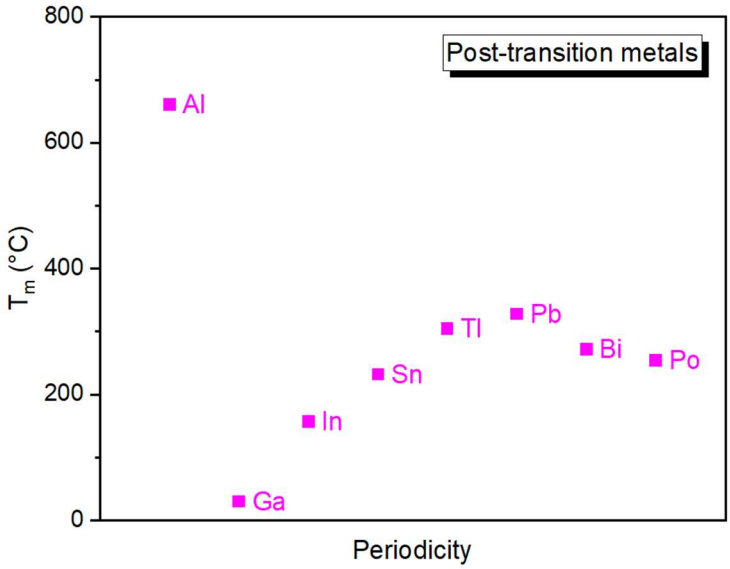

Fig. S5. The melting points of different metals in post-transition metals.

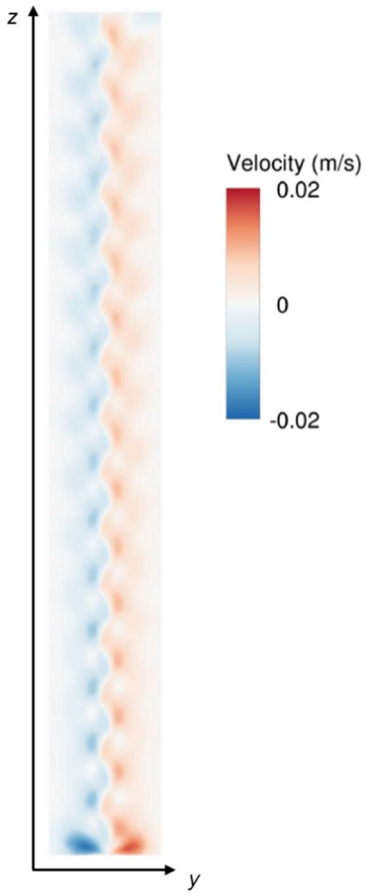

Fig. S6. Full-scale two-dimensional transient distribution of the flow field in the y-direction at the operation time of 0.1 s. The light orange color represents the positive direction (right), and the light blue color represents the negative direction (left).

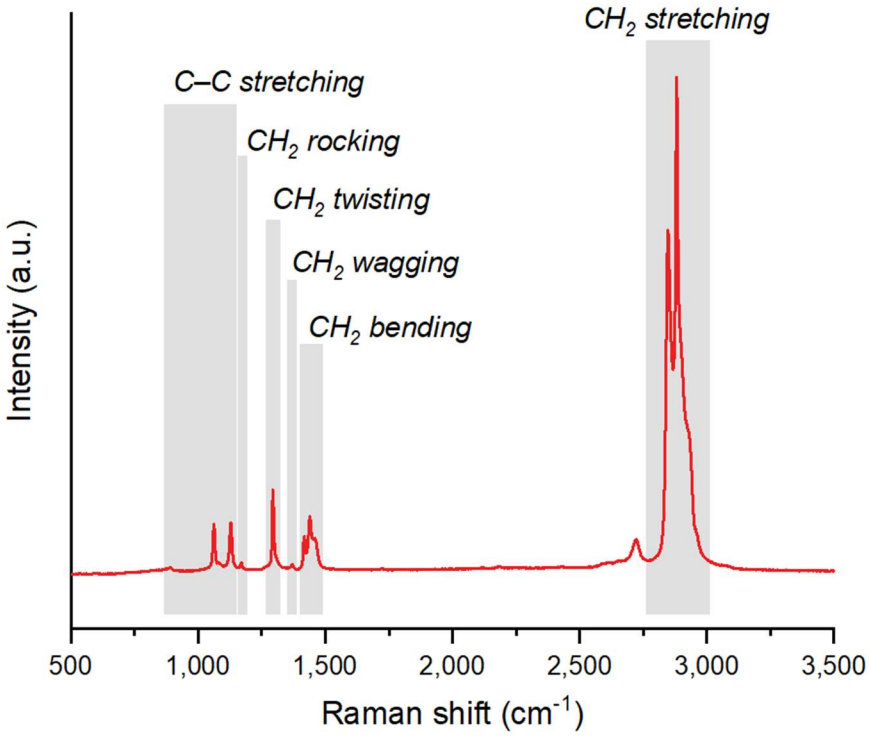

Fig. S7. Structural resolution of PE by Raman spectroscopy.

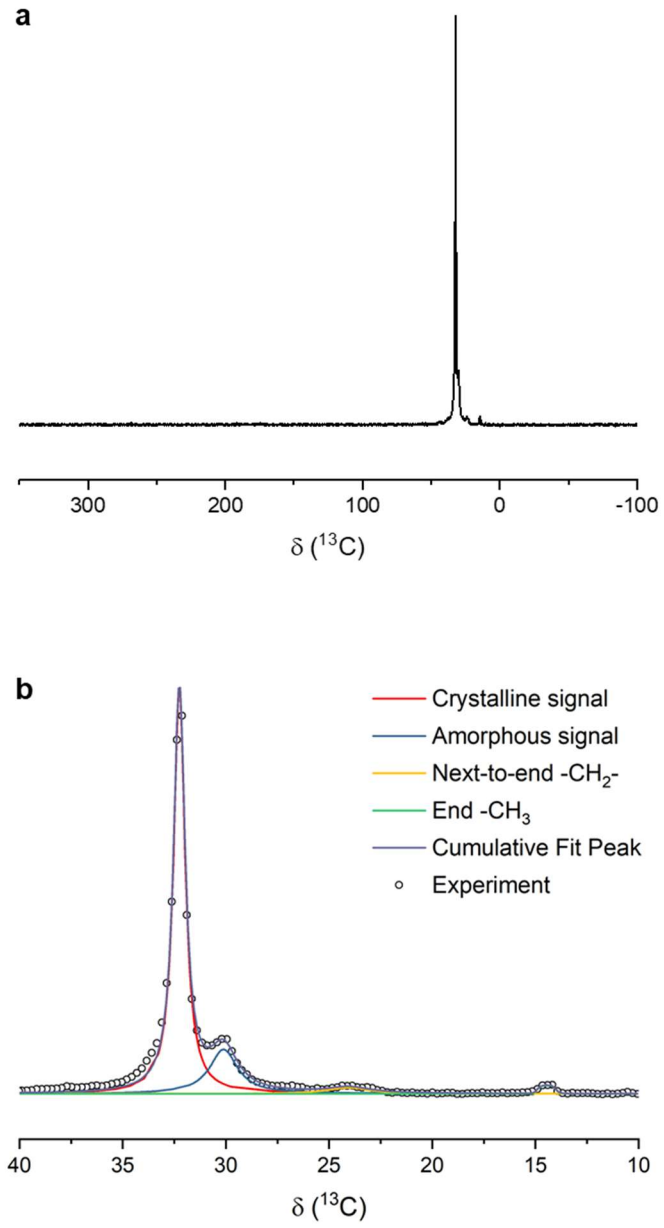

Fig. S8. ^{13}C CP/MAS/TOSS NMR spectra of PE. (a) Full-scale ^{13}C NMR spectra of PE. (b) Magnified view of the ^{13}C NMR spectra of PE with peak fitting to identify the specific structure.

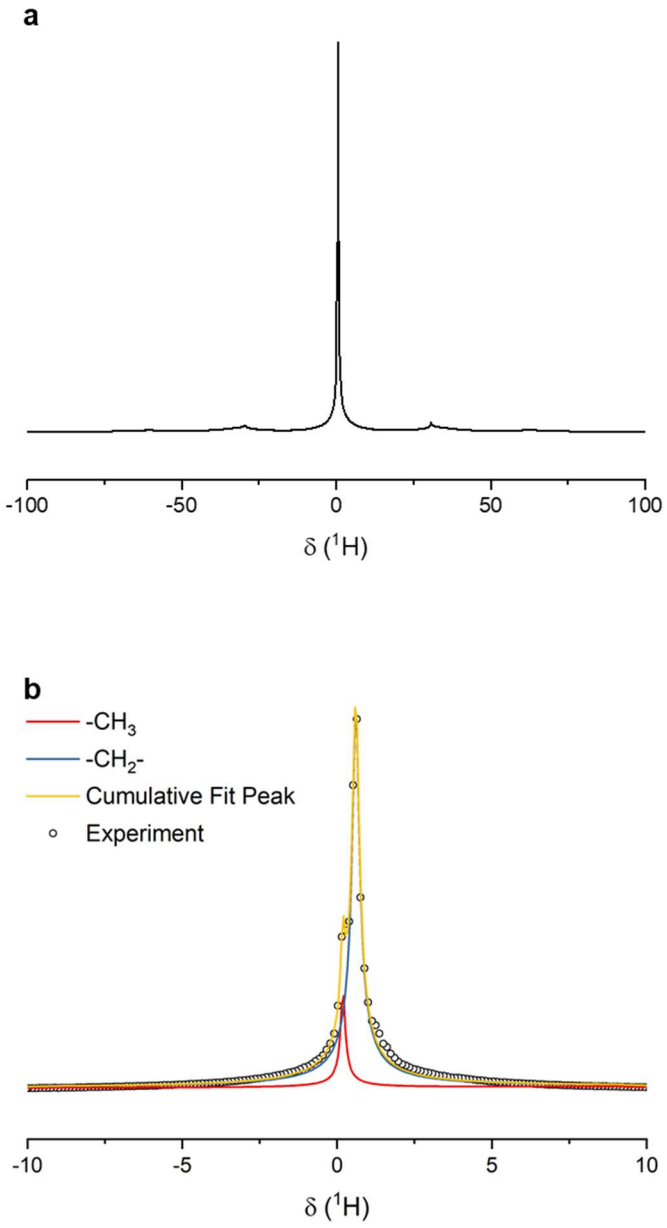

Fig. S9. ^{1}H MAS NMR spectra of PE. (a) Full-scale ^{1}H NMR spectra of PE. (b) Magnified view of the ^{1}H NMR spectra of PE with peak fitting to identify the specific structure.

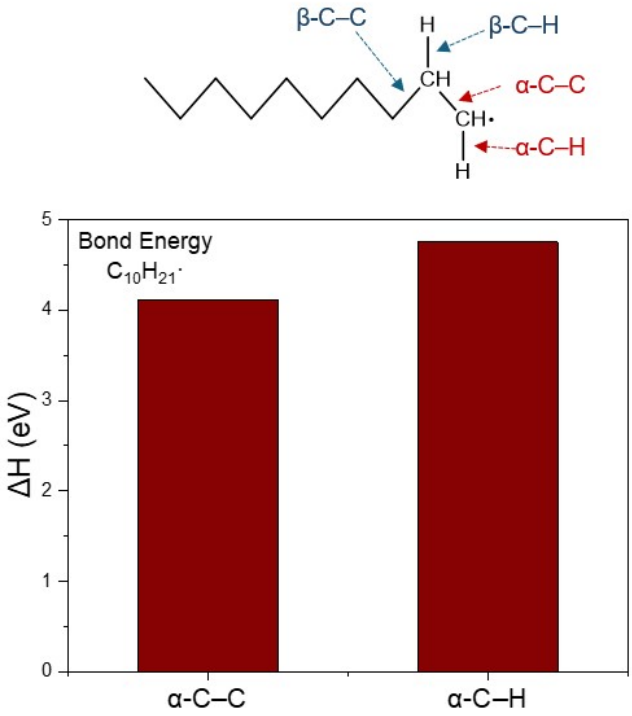

Fig. S10. The bond energy of α-C–C and α-C–H in C_{10}·.

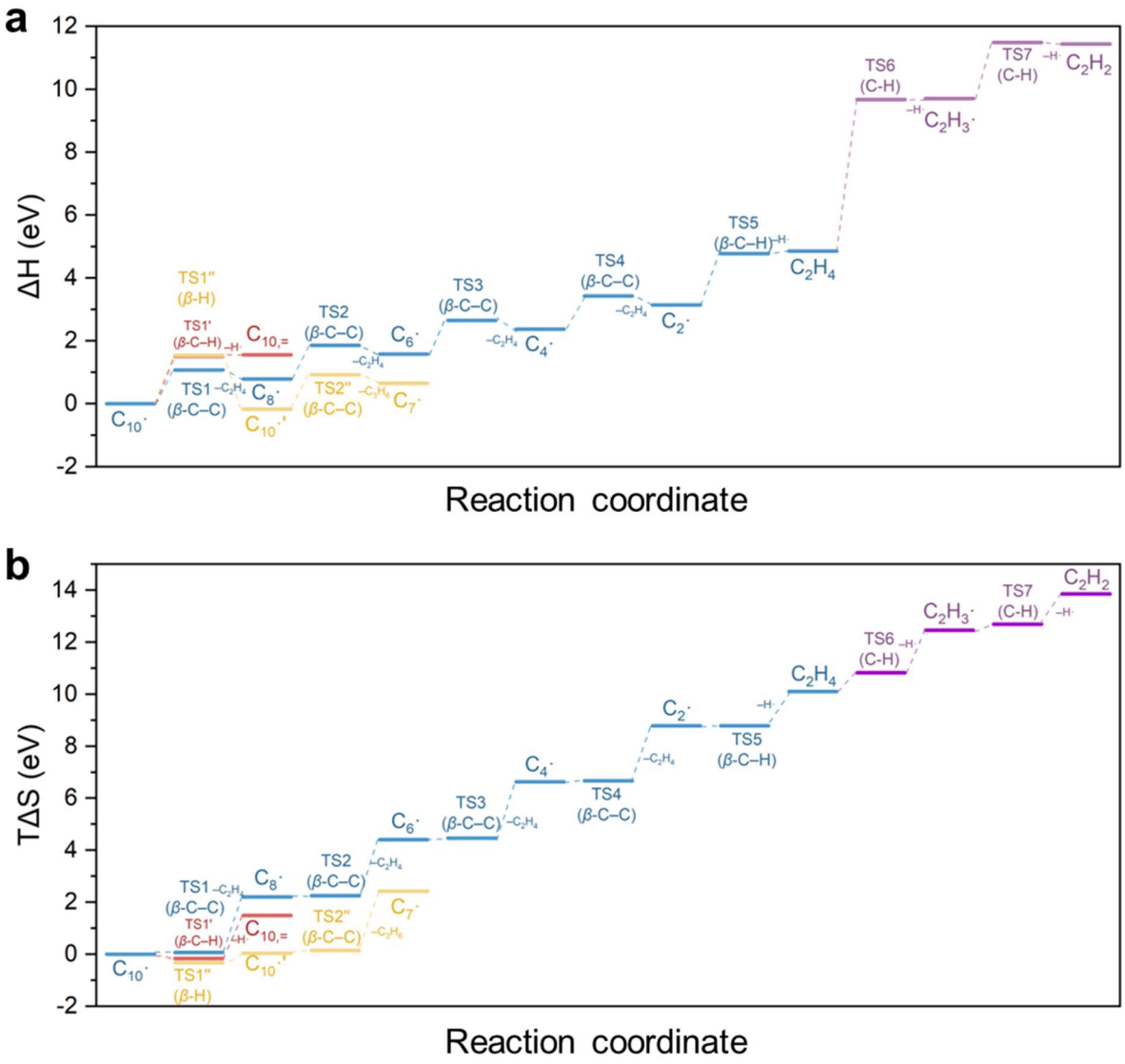

Fig. S11. The enthalpy (ΔH) and entropy (TΔS) diagram for gas-phase reaction of n-decyl radical at 1250 °C and 1 atm.

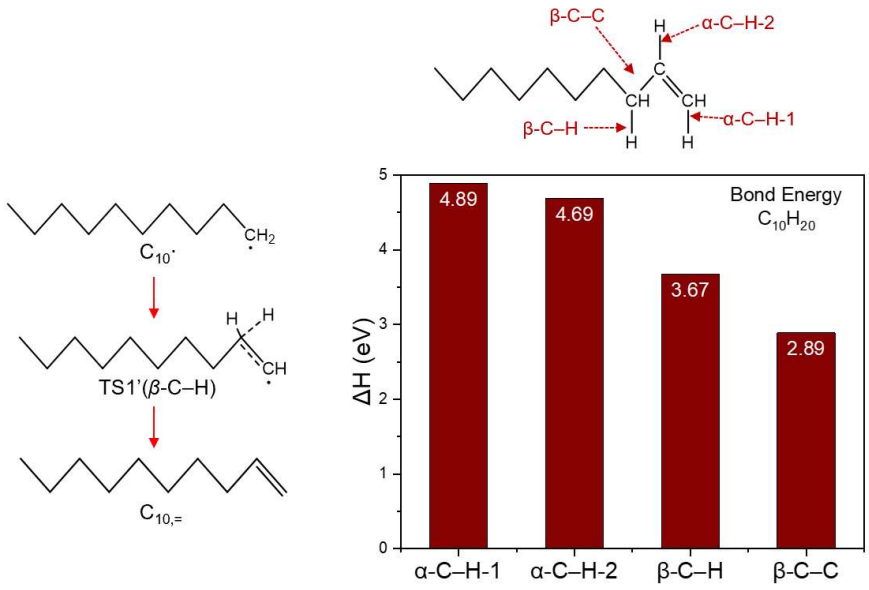

Fig. S12. The scheme of the formation of 1-decene from n-decyl radical and the bond energies of 1-decene.

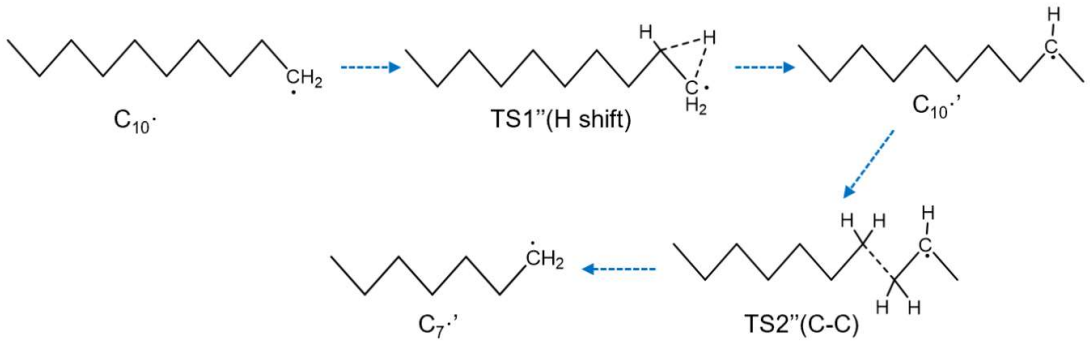

Fig. S13. The scheme of producing propane from n-decyl radical via C_{10}'.

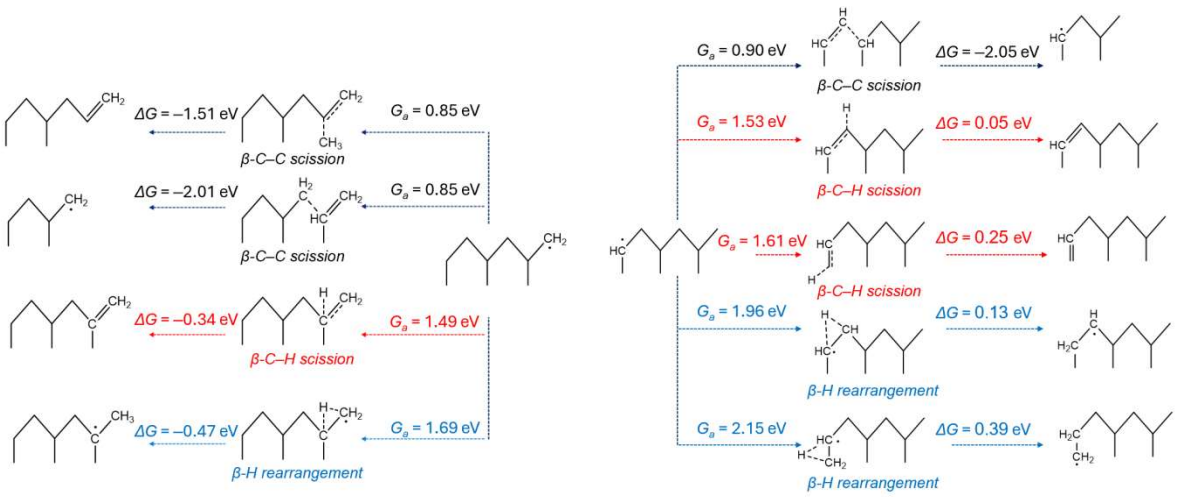

Fig. S14. DFT-derived free-energy change of β-C–C bond scissions, β-C–H bond scissions, and β-H rearrangements of two kinds of $(C_3H_7)_3\cdot$ radicals.

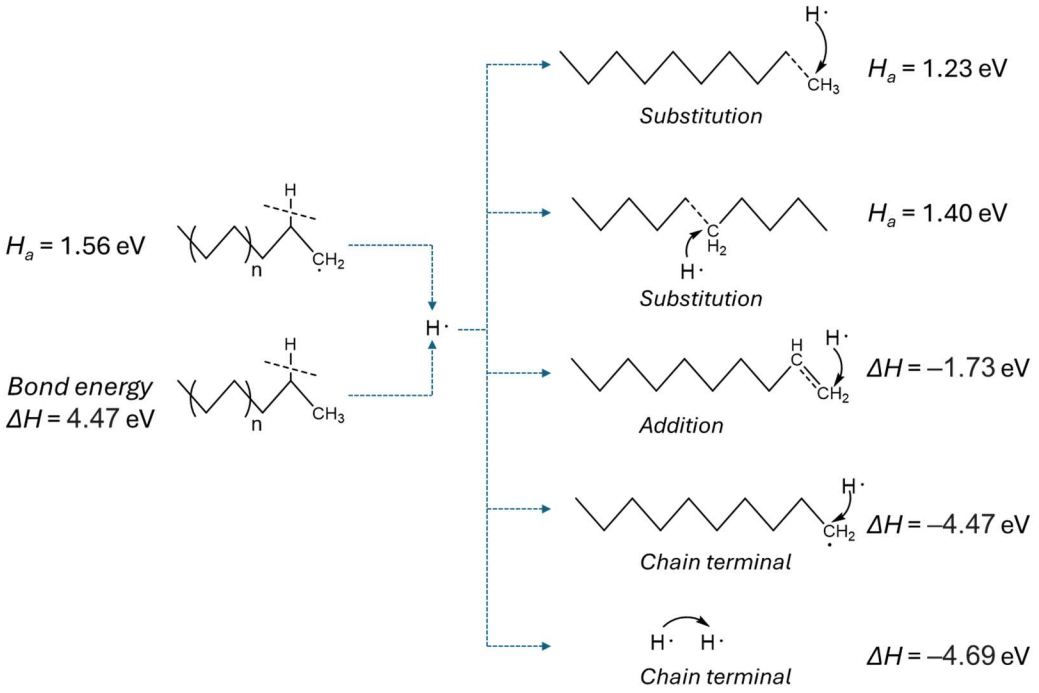

Fig. S15. The evolution of H· radical in the gas phase.

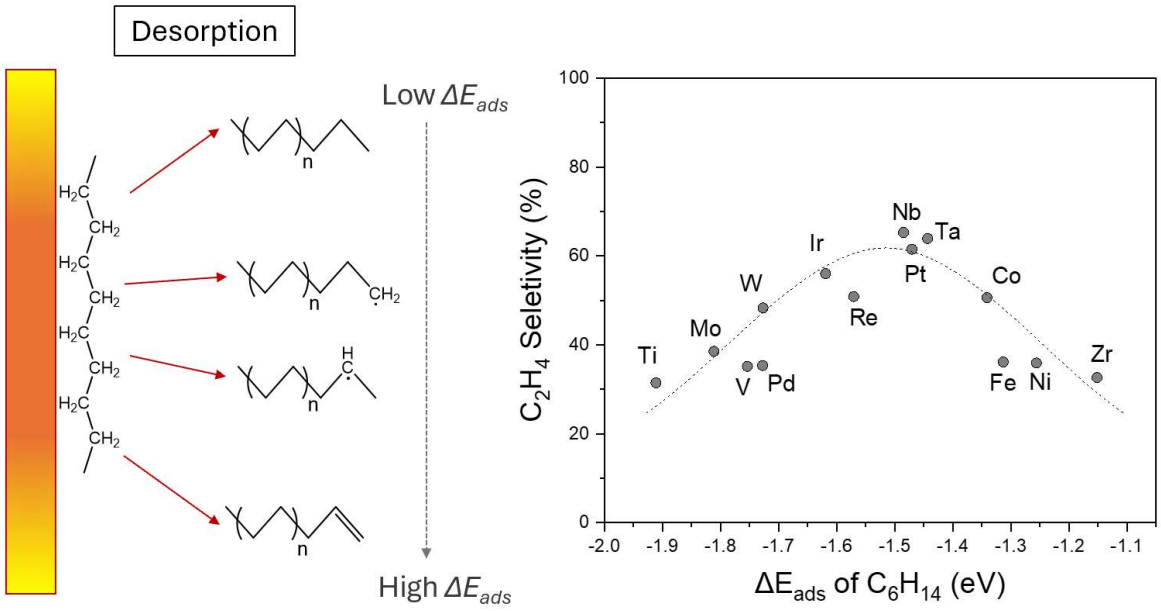

Fig. S16. The effect of C_6H_{14} adsorption energy on the metal surface on the C_2H_4 selectivity.

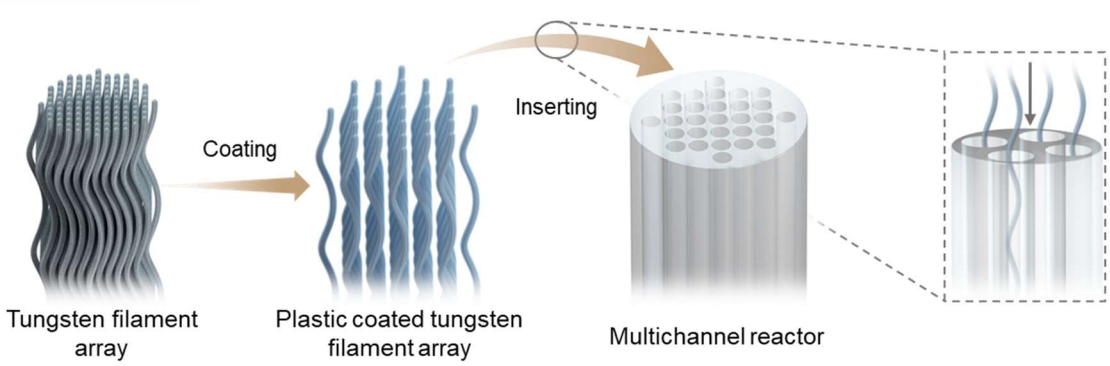

Fig. S17. Schematic of a proposed potentially larger scale application of this method by incorporating current industrial process that involves metal processing, enameled wire processing, and mechanical processing.

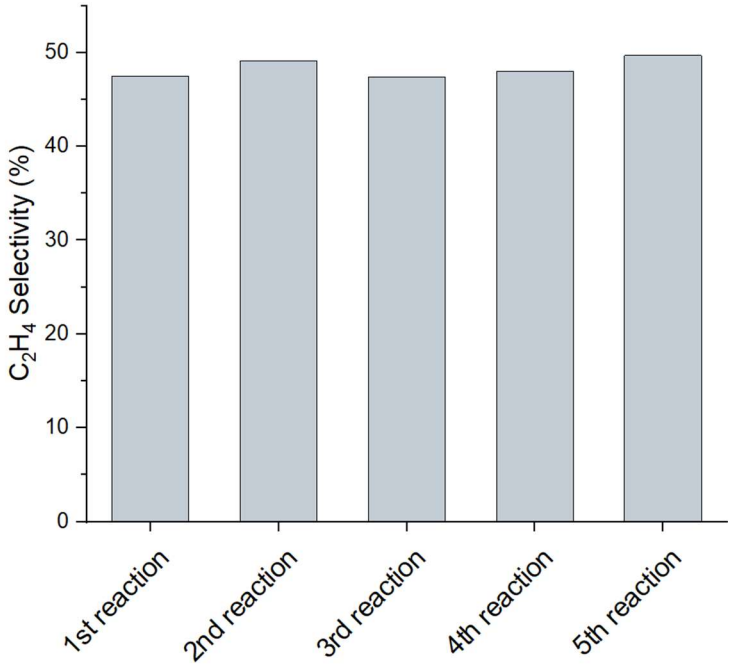

Fig. S18. Ethylene selectivity for cyclic experiments of the depolymerization reaction of polyethylene from five consecutive reactions.

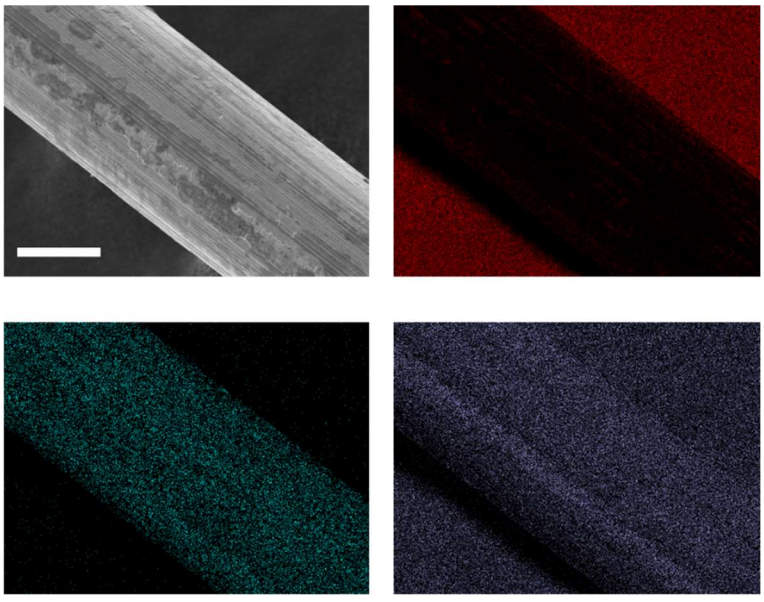

Fig. S19. SEM image and EDS mapping of fresh tungsten filament before reaction with scale bar of 50 µm. In EDS mapping, red, cyan, and lavender colors represent carbon, tungsten, and oxygen, respectively. The background of the tungsten filament is a conductive tape containing the elements of carbon and oxygen. The gap between the tungsten filament and the conductive tape on the lower left side is caused by the partial blocking of the X-ray signal of the energy dispersive spectrometer probe by the vertical height of the tungsten filament.

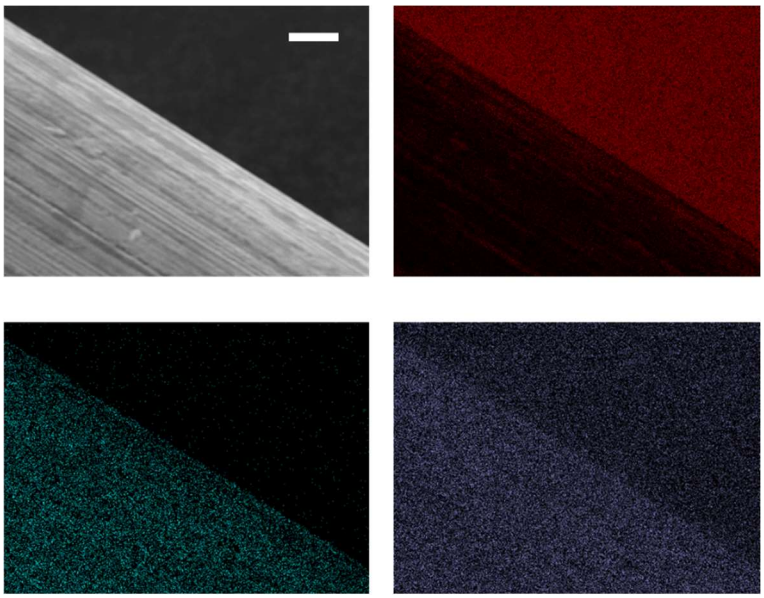

Fig. S20. SEM image and EDS mapping of fresh tungsten filament before reaction with scale bar of 10 µm. In EDS mapping, red, cyan, and lavender colors represent carbon, tungsten, and oxygen, respectively. The background of the tungsten filament is a conductive tape containing the elements of carbon and oxygen.

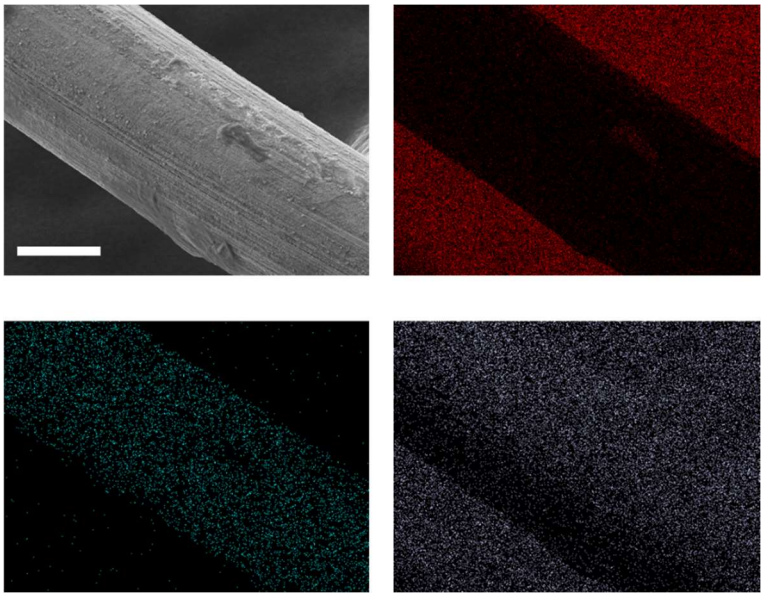

Fig. S21. SEM image and EDS mapping of used tungsten filament after reaction with scale bar of 50 µm. In EDS mapping, red, cyan, and lavender colors represent carbon, tungsten, and oxygen, respectively. The background of the tungsten filament is a conductive tape containing the elements of carbon and oxygen. The gap between the tungsten filament and the conductive tape on the lower left side is caused by the partial blocking of the X-ray signal of the energy dispersive spectrometer probe by the vertical height of the tungsten filament.

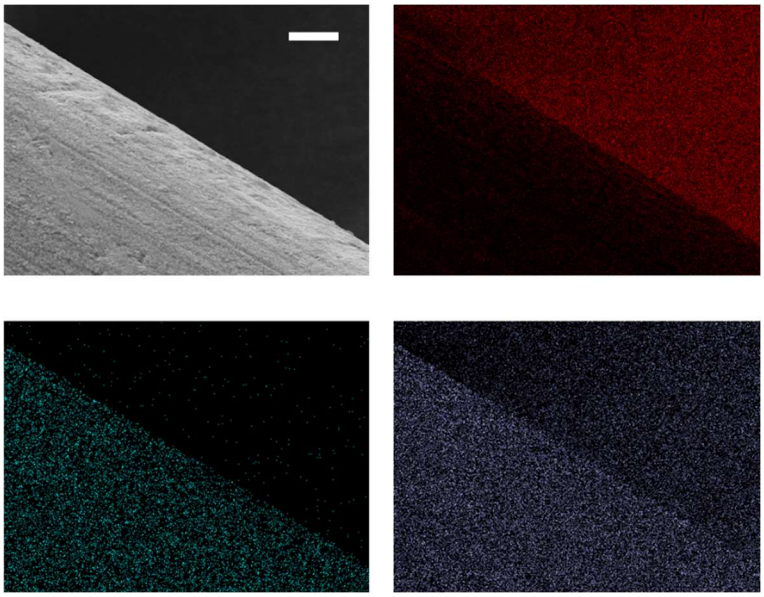

Fig. S22. SEM image and EDS mapping of used tungsten filament after reaction with scale bar of 10 μm. In EDS mapping, red, cyan, and lavender colors represent carbon, tungsten, and oxygen, respectively. The background of the tungsten filament is a conductive tape containing the elements of carbon and oxygen.

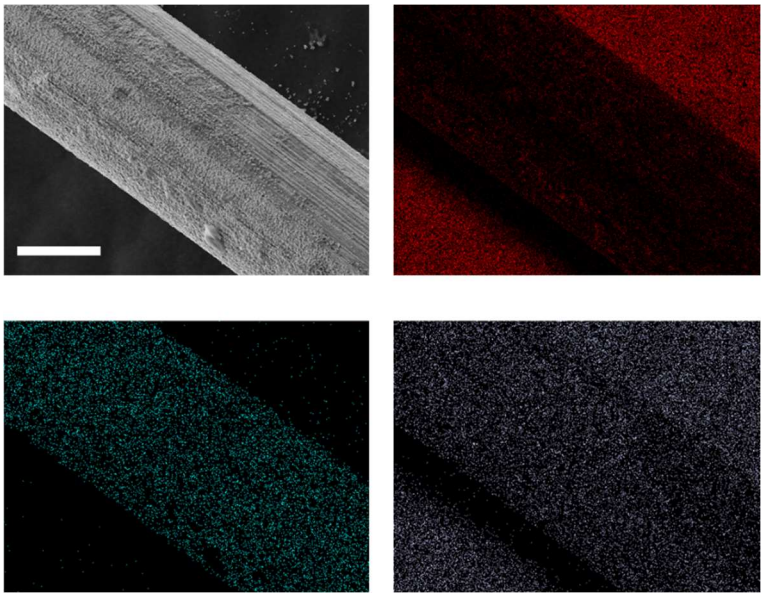

Fig. S23. SEM image and EDS mapping of used tungsten filament after the tenth reaction with scale bar of 50 µm. In EDS mapping, red, cyan, and lavender colors represent carbon, tungsten, and oxygen, respectively. The background of the tungsten filament is a conductive tape containing the elements of carbon and oxygen. The gap between the tungsten filament and the conductive tape on the lower left side is caused by the partial blocking of the X-ray signal of the energy dispersive spectrometer probe by the vertical height of the tungsten filament.

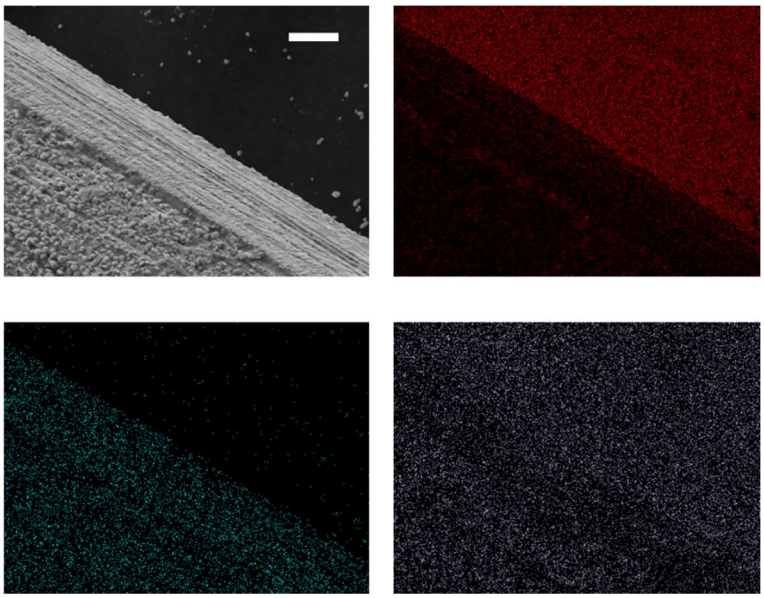

Fig. S24. SEM image and EDS mapping of used tungsten filament after the tenth reaction with scale bar of 10 µm. In EDS mapping, red, cyan, and lavender colors represent carbon, tungsten, and oxygen, respectively. The background of the tungsten filament is a conductive tape containing the elements of carbon and oxygen.

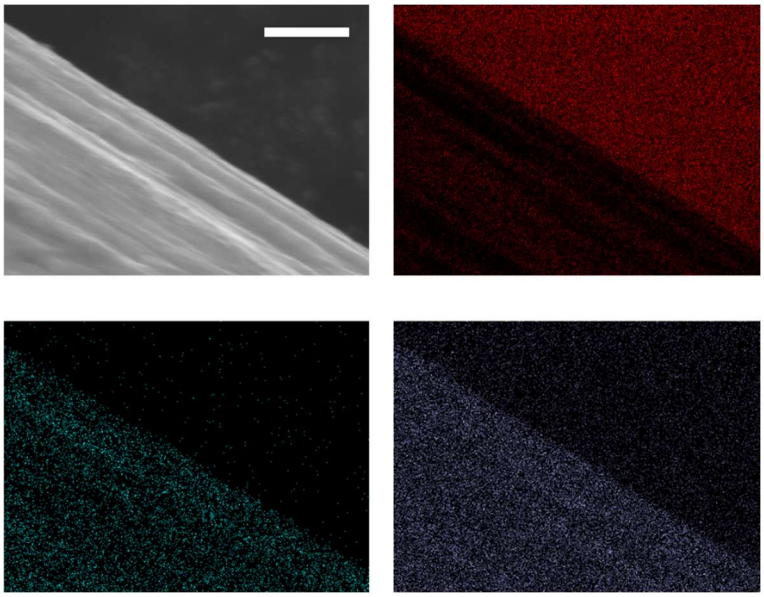

Fig. S25. SEM image and EDS mapping of fresh tungsten filament before reaction with scale bar of 2 µm. In EDS mapping, red, cyan, and lavender colors represent carbon, tungsten, and oxygen, respectively. The background of the tungsten filament is a conductive tape containing the elements of carbon and oxygen.

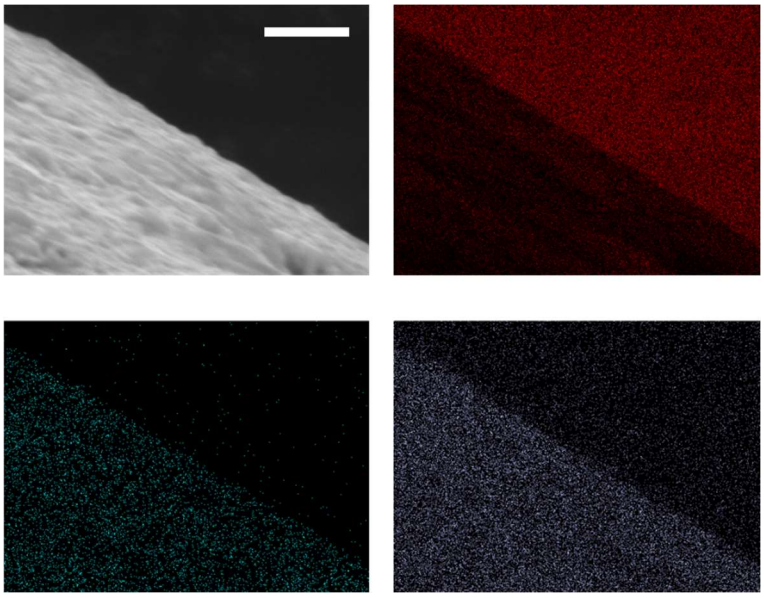

Fig. S26. SEM image and EDS mapping of used tungsten filament after the first reaction with scale bar of 2 μm. In EDS mapping, red, cyan, and lavender colors represent carbon, tungsten, and oxygen, respectively. The background of the tungsten filament is a conductive tape containing the elements of carbon and oxygen.

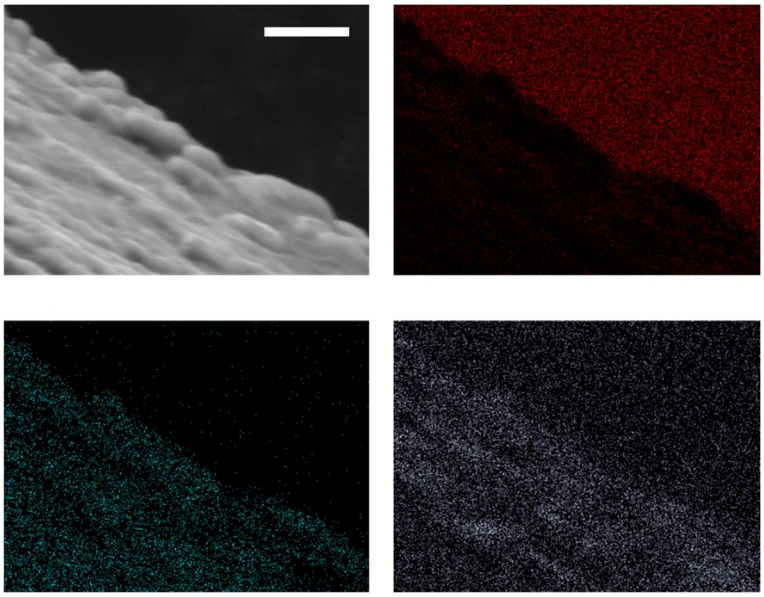

Fig. S27. SEM image and EDS mapping of used tungsten filament after the tenth reaction with scale bar of 2 μm. In EDS mapping, red, cyan, and lavender colors represent carbon, tungsten, and oxygen, respectively. The background of the tungsten filament is a conductive tape containing the elements of carbon and oxygen.

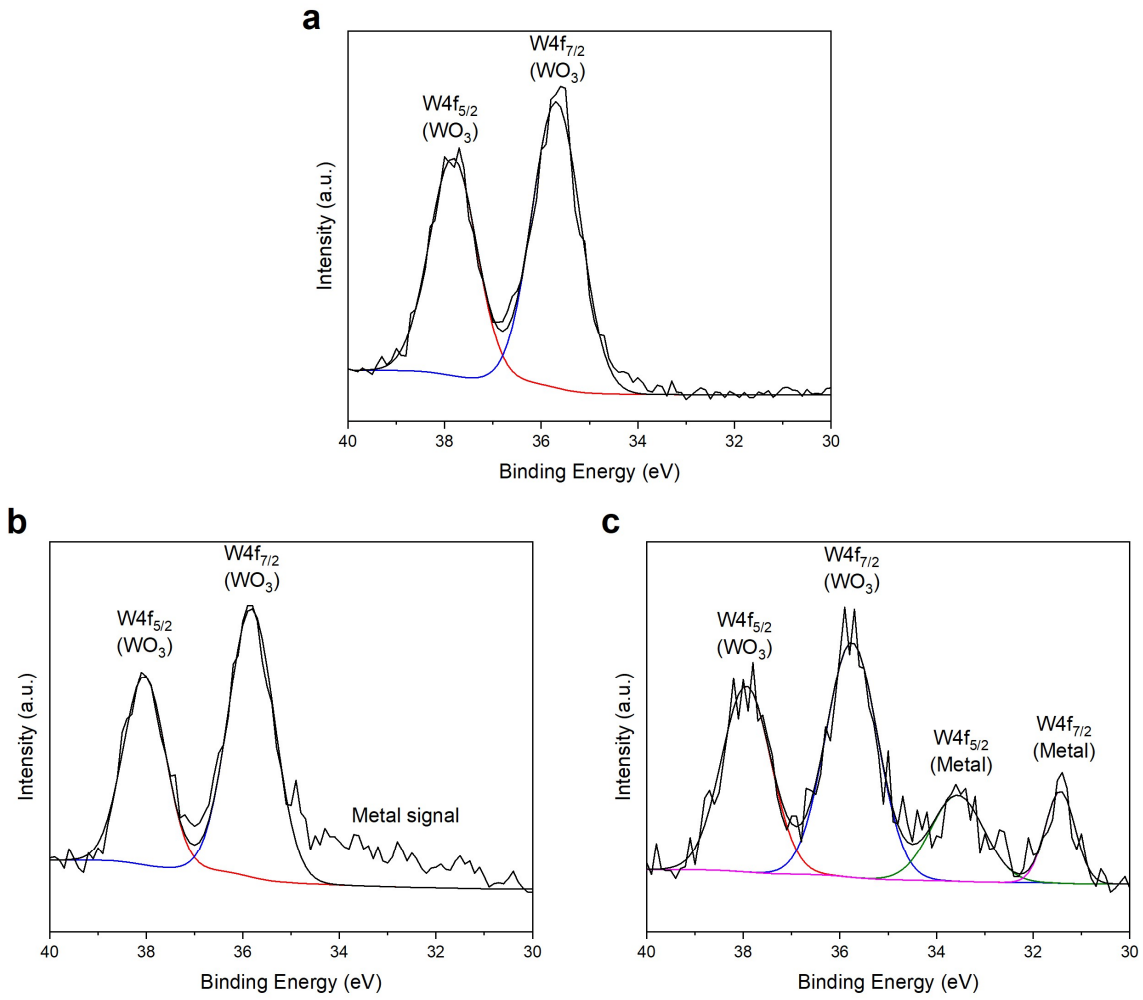

Fig. S28. Surface chemical valence of tungsten filaments before and after the reaction by W 4f XPS spectra. (a) Fresh tungsten filament before reaction with only tungsten oxide signals (W $4f_{5/2}$ and W $4f_{7/2}$). (b) Used tungsten filament after the first reaction with tungsten oxide signals (W $4f_{5/2}$ and W $4f_{7/2}$) and slight tungsten metal signal. (c) Used tungsten filament after the tenth reaction with tungsten oxide signals (W $4f_{5/2}$ and W $4f_{7/2}$) and tungsten metal signals (W $4f_{5/2}$ and W $4f_{7/2}$).

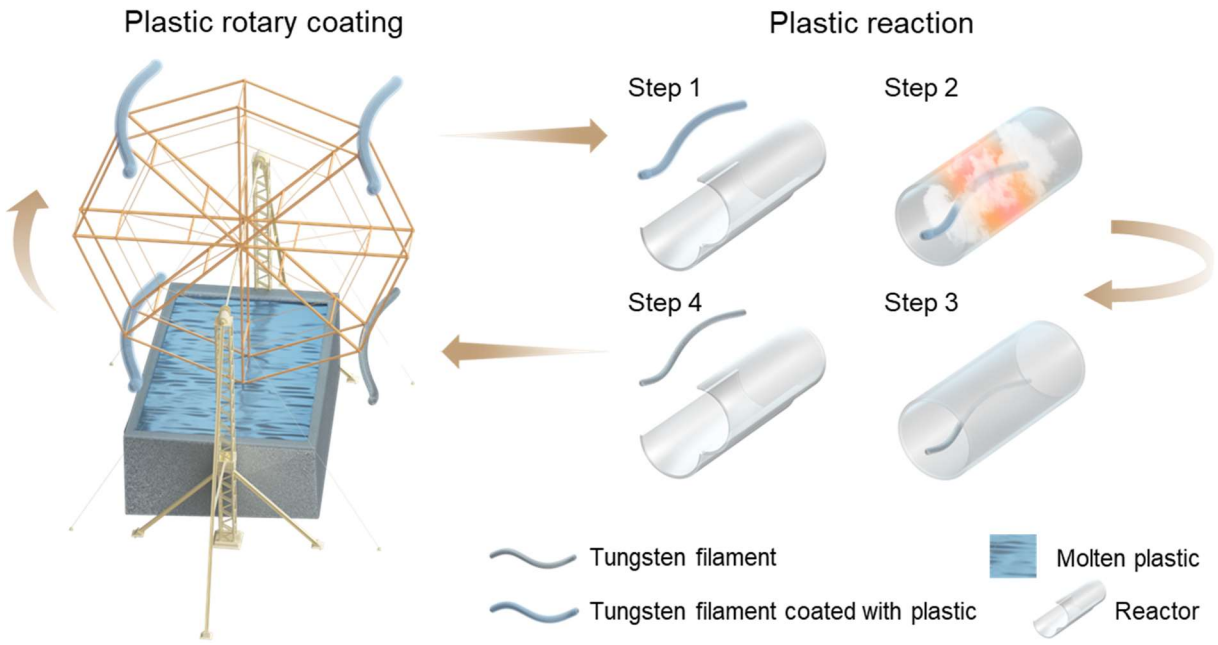

Fig. S29. Schematic of a proposed Ferris wheel-like continuous plant concept based on this approach for plastic depolymerization. This figure illustrates a proposed Ferris wheel-like continuous plant concept. The unit consists of three parts, i.e., a plastic melting system, a tungsten rotary coating system, and a reaction system. In this continuous reaction unit, PE plastics of any shape are melted without mechanical pre-processing (e.g., shredding). Through the rotation of a Ferris wheel-like rotary coating system, tungsten filament is submerged into molten plastic for coating. When the tungsten filament, already coated with plastic, reaches the right side of the rotary coating system, it is delivered into the reaction system for depolymerization reaction, and sent back for the next round of coating after the reaction.

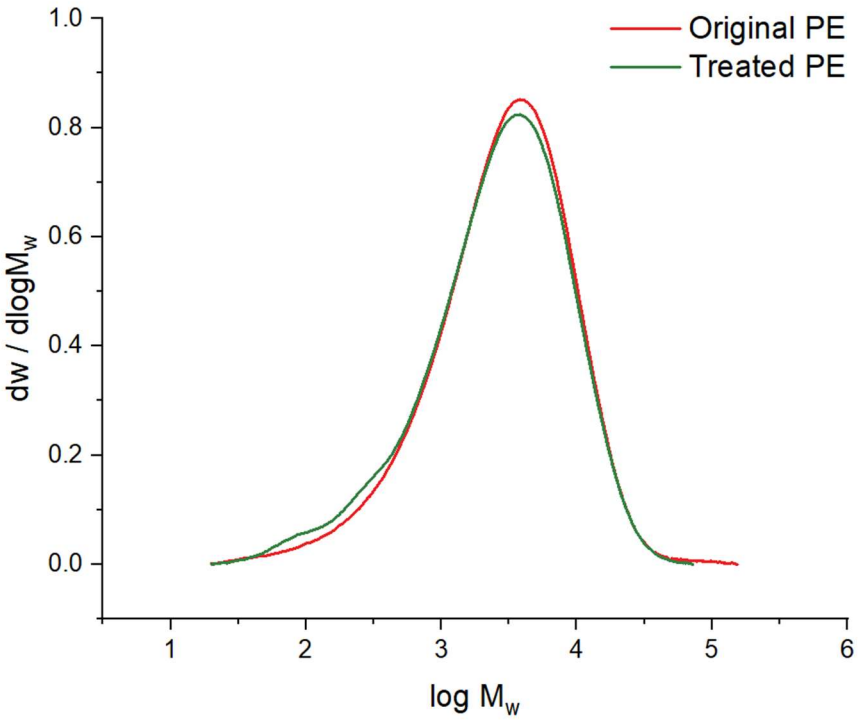

Fig. S30. Comparison of HT-GPC chromatograms of original PE and treated PE.

Supplementary Tables

Table S1. Detailed elemental composition of PE.

	Elemental composition
C (%)	85.15
H (%)	14.01
O (%)[a]	0.62
N (%)	0.22
S (%)	ND[b]

a: Calculated by difference; b: not detected.

Table S2. Band assignments of Raman spectroscopy of PE.

Bands (cm^{-1})	Assignments
2881	CH_2 asymmetric stretching
2847	CH_2 symmetric stretching
1458	CH_2 bending
1439	CH_2 bending
1418	CH_2 bending
1369	CH_2 wagging
1294	CH_2 twisting
1169	CH_2 rocking
1128	C–C symmetric stretching
1083	C–C stretching
1063	C–C asymmetric stretching
893	C–C stretching (branches)

Table S3. Peak fitting parameters of the ^{13}C NMR spectra of PE.

Chemical shift (ppm)	Assignments	FWHM (ppm)	Peak shape	Amount (%)
32.3	Crystalline region	0.67	GL*	75.2
30.1	Amorphous region	1.64	GL	19.5
24.1	Next-to-end CH_2	2.49	GL	4.0
14.5	End CH_3	0.91	GL	1.3

*: Gaussian/Lorentzian line shape

Table S4. Peak fitting parameters of the ^{1}H NMR spectra of PE.

Chemical shift (ppm)	Assignments	FWHM (ppm)	Peak shape	Amount (%)
0.60	$-CH_2-$	0.38	LA*	86.4
0.19	$-CH_3$	0.2	LA	13.6

*: Lorentzian Asymmetric line shape

Table S5. XPS peak fitting parameters for tungsten filaments after different conditions.

Sample	Species	Binding energy (eV)	FWHM (ppm)	Peak shape	Amount (%)
Fresh tungsten filament	$W4f_{5/2}$ (WO_3)	37.8	1.15	GL*	42.8
	$W4f_{7/2}$ (WO_3)	35.7	1.17	GL	57.2
Tungsten filament after 1st reaction	$W4f_{5/2}$ (WO_3)	38.0	1.02	GL	39.4#
	$W4f_{7/2}$ (WO_3)	35.8	1.12	GL	60.6#
Tungsten filament after 10th reaction	$W4f_{5/2}$ (WO_3)	37.9	1.20	GL	32.0
	$W4f_{7/2}$ (WO_3)	35.8	1.26	GL	42.3
	$W4f_{5/2}$ (Metal)	33.6	1.30	GL	16.1
	$W4f_{7/2}$ (Metal)	31.4	0.73	GL	9.6

*: Gaussian/Lorentzian line shape.

#: This amount represents only the percentage of peaks that have been split and fitted, and does not indicate the percentage of all species.

Table S6. Comparison of molecular weight and its distribution of original PE and treated PE.

Sample	M_n	M_w	$Đ$
Original PE	1261	5162	4.1
Treated PE	1257	4892	3.9

Table S7. Comparison of conventional catalytic pyrolysis results in the literature and this work.

Catalyst (with reaction environment)	Ethylene selectivity (%)	Reference
HZSM-5 zeolite	9.45	23
HZSM-5 zeolite	3.55	23
HZSM-5 zeolite	1.46	23
HZSM-5 zeolite	1.10	24
HZSM-5 zeolite	1.41	24
HZSM-5 zeolite	1.83	24
HZSM-5 zeolite	2.70	25
Clinoptilolite containing rhyolite tuff	0.43	24
Clinoptilolite containing rhyolite tuff	0.66	24
Clinoptilolite containing rhyolite tuff	0.69	24
Equilibrium fluid catalytic cracking catalyst	0.62	24
Equilibrium fluid catalytic cracking catalyst	0.50	24
Equilibrium fluid catalytic cracking catalyst	0.65	24
MgO with microwave	17.63	26
MgO with microwave	17.80	26
MgO with microwave	15.64	26
MgO with microwave	16.92	26
MgO with microwave	5.12	26

MgO with microwave	7.71	26
MgO with microwave	16.09	26
MgO with microwave	15.61	26
MgO with microwave	16.72	26
MgO with microwave	11.65	26
MgO with microwave	13.46	26
MgO with microwave	15.44	26
MgO with microwave	17.70	26
MgO with microwave	18.65	26
HY zeolite	0.62	27
ZSM-5 Zeolite	1.13	28
ZSM-5 Zeolite	1.64	28
ZSM-5 Zeolite	2.69	28
ZSM-5 Zeolite	5.15	28
ZSM-5 Zeolite	6.74	28
ZSM-5 Zeolite	7.51	29
Y-Zeolite	0.51	28
Y-Zeolite	0.92	28
Y-Zeolite	1.34	28
Y-Zeolite	1.82	28
Y-Zeolite	2.92	28

HUSY Zeolite	0.30	25
HMOR Zeolite	1.40	25
SAHA	0	25
MCM-41	0	25
Non-catalyzed	4.91	30
This work	48.32	-
This work	65.28	-
This work	63.90	-
This work	63.29	-

Table S8. Physical parameters used in the CFD numerical simulation.

Physical parameters	Symbol	Value
Gravity, m s^{-2}	g	9.8
Density of argon, kg m^{-3}	ρ_f	Ideal gas law
Specific heat of argon, J kg^{-1} °C^{-1}	c_{pf}	520.64
Thermal conductivity of argon, W m^{-1} °C^{-1}	λ_f	0.0158
Viscosity of argon, kg m^{-1} s^{-1}	μ_f	2.125×10^{-5}
Density of tungsten, kg m^{-3}	ρ_t	19300
Specific heat of tungsten, J kg^{-1} °C^{-1}	c_{pt}	129.12
Thermal conductivity of tungsten, W m^{-1} °C^{-1}	λ_t	172.4
Density of quartz, kg m^{-3}	ρ_q	2648
Specific heat of quartz, J kg^{-1} °C^{-1}	c_{pq}	670
Thermal conductivity of quartz, W m^{-1} °C^{-1}	λ_q	1.4

Table S9. Life cycle inventory.

Impact Category	Energy consumption (MJ per unit)	GHG emission (kg CO_2e per unit)	Water consumption (tonne per unit)
Grinding	435.24	62.07	0.09
Coating	761.59	108.60	0.16
Reaction	6854.30	977.42	1.41
Fabrication and extrusion	65409	1612.27	6.84
Incineration	304.34	3024.7	0.66
Nitrogen	3065	184.58	0.93
Pyrolysis	25287.93	3606.06	5.20

References

1. Forsythe, W. E. & Watson, E. M. Resistance and Radiation of Tungsten as a Function of Temperature. *J. Opt. Soc. Am.* **24**, 114-118 (1934).
2. Desai, P. D., Chu, T. K., James, H. M. & Ho, C. Y. Electrical Resistivity of Selected Elements. *J. Phys. Chem. Ref. Data* **13**, 1069-1096 (1984).
3. Ebeling, M. E. The Dumas Method for Nitrogen in Feeds. *J. AOAC Int.* **51**, 766-770 (1968).
4. Jung, S. *et al.* Comparison of kjeldahl and dumas methods for determining protein contents of soybean products. *J. Am. Oil Chem. Soc.* **80**, 1169-1173 (2003).
5. Beamson, G. & Briggs, D. *High resolution XPS of organic polymers: the scienta ESCA300 database*. (Wiley, 1992).
6. Agrawal, D. C. The coiling factor in the tungsten filament lamps. *Lat. Am. J. Phys. Educ.* **5**, 21 (2011).
7. Rajendra, N. Study on Emitted Radiations from Filament Bulb of Different Power. *J. Appl. Math. Phys.* **08**, 1615-1645 (2020).
8. Forsythe, W. E. & Worthing, A. G. The properties of tungsten and the characteristics of tungsten lamps. *Astrophys. J.* **61**, 146 (1925).
9. Gaussian 16 Rev. B.01 (Wallingford, CT, 2016).
10. Lee, C., Yang, W. & Parr, R. G. Development of the Colle-Salvetti correlation-energy formula into a functional of the electron density. *Phys Rev B Condens Matter* **37**, 785-789 (1988).

11. Grimme, S., Antony, J., Ehrlich, S. & Krieg, H. A consistent and accurate ab initio parametrization of density functional dispersion correction (DFT-D) for the 94 elements H-Pu. *J. Chem. Phys.* **132**, 154104 (2010).

12. Lu, T. & Chen, F. Multiwfn: A multifunctional wavefunction analyzer. *J. Comput. Chem.* **33**, 580-592 (2012).

13. Jain, A. *et al.* Commentary: The Materials Project: A materials genome approach to accelerating materials innovation. *APL Materials* **1**, 011002 (2013).

14. Kresse, G. & Hafner, J. Ab initio molecular dynamics for open-shell transition metals. *Phys Rev B Condens Matter* **48**, 13115-13118 (1993).

15. Kresse, G. & Hafner, J. Ab initio molecular-dynamics simulation of the liquid-metal-amorphous-semiconductor transition in germanium. *Phys Rev B Condens Matter* **49**, 14251-14269 (1994).

16. Kresse, G. & Furthmuller, J. Efficient iterative schemes for ab initio total-energy calculations using a plane-wave basis set. *Phys Rev B Condens Matter* **54**, 11169-11186 (1996).

17. Kresse, G. & Furthmuller, J. Efficiency of ab-initio total energy calculations for metals and semiconductors using a plane-wave basis set. *Computational Materials Science* **6**, 15-50 (1996).

18. Perdew, J. P., Burke, K. & Ernzerhof, M. Generalized Gradient Approximation Made Simple. *Phys. Rev. Lett.* **77**, 3865-3868 (1996).

19. Grimme, S. Semiempirical GGA-type density functional constructed with a long-range dispersion correction. *J. Comput. Chem.* **27**, 1787-1799 (2006).

20. Li, H. *et al.* Toward carbon-neutral ethylene production: assessment of the application potential of bio-ethylene production pathways in China. *Biofuels, Bioprod. Biorefin.* **16**, 1568-1582 (2022).

21. Martín-Lara, M. A., Moreno, J. A., Garcia-Garcia, G., Arjandas, S. & Calero, M. Life cycle assessment of mechanical recycling of post-consumer polyethylene flexible films based on a real case in Spain. *J. Cleaner Prod.* **365**, 132625 (2022).

22. Meran, C., Ozturk, O. & Yuksel, M. Examination of the possibility of recycling and utilizing recycled polyethylene and polypropylene. *Materials & Design* **29**, 701-705 (2008).

23. Artetxe, M. *et al.* Cracking of High Density Polyethylene Pyrolysis Waxes on HZSM-5 Catalysts of Different Acidity. *Ind. Eng. Chem. Res.* **52**, 10637-10645 (2013).

24. Miskolczi, N., Bartha, L., Deák, G., Jóver, B. & Kalló, D. Thermal and thermo-catalytic degradation of high-density polyethylene waste. *J. Anal. Appl. Pyrolysis* **72**, 235-242 (2004).

25. Lin, Y. H., Sharratt, P. N., Garforth, A. A. & Dwyer, J. Catalytic Conversion of Polyolefins to Chemicals and Fuels over Various Cracking Catalysts. *Energy Fuels* **12**, 767-774 (1998).

26. Fan, L. *et al.* Ex-situ catalytic upgrading of vapors from microwave-assisted pyrolysis of low-density polyethylene with MgO. *Energy Convers. Manage.* **149**, 432-441 (2017).

27. Elordi, G. *et al.* Catalytic pyrolysis of high density polyethylene in a conical spouted bed reactor. *J. Anal. Appl. Pyrolysis* **79**, 450-455 (2007).

28. Bagri, R. & Williams, P. T. Catalytic pyrolysis of polyethylene. *J. Anal. Appl. Pyrolysis* **63**, 29-41 (2002).

29. Li, X. *et al.* Improving the aromatic production in catalytic fast pyrolysis of cellulose by co-feeding low-density polyethylene. *Appl. Catal. A: Gen.* **455**, 114-121 (2013).

30. Encinar, J. M. & González, J. F. Pyrolysis of synthetic polymers and plastic wastes. Kinetic study. *Fuel Process. Technol.* **89**, 678-686 (2008).